

**Turbulent viscosity and turbulent magnetic diffusivity in a decaying spin-down flow of liquid sodium**Vitaliy Noskov,<sup>1</sup> Sergey Denisov,<sup>1</sup> Rodion Stepanov,<sup>1,2</sup> and Peter Frick<sup>1,2,\*</sup><sup>1</sup>*Institute of Continuous Media Mechanics, Korolyov 1, RU-614013 Perm, Russia*<sup>2</sup>*Dep. of Applied Math. and Mech., State National Research Polytechnical University of Perm, Komsomolskii av. 29, RU-614990 Perm, Russia*

(Received 27 June 2011; revised manuscript received 10 October 2011; published 4 January 2012)

The free decay of a strong flow of liquid sodium (at Reynolds number defined via the maximal mean velocity and the radius of the channel cross section up to  $Re \approx 3 \times 10^6$  and the corresponding magnetic Reynolds number up to  $Rm \approx 30$ ) generated by the sudden stop of a rapidly rotating toroidal channel is studied experimentally. The toroidal and poloidal components of velocity are measured using a potential probe. We describe the onset of motion, the evolution of strongly anisotropic fluctuations, and the homogenization and decay of turbulence in the final period. We analyze the statistical characteristics of velocity fields in relation to the behavior of effective magnetic diffusivity estimated from measurements of the phase shift between the induced and applied magnetic fields. For the late (self-similar) decay of turbulent flow, turbulent viscosity is shown to be dependent on the root-mean-square velocity pulsations and can be expressed as  $\nu_t \sim \nu Re^{1.3}$ . The behavior of turbulent magnetic diffusivity depends on the magnetic Reynolds number defined in terms of the root-mean-square velocity pulsations. At low magnetic Reynolds numbers ( $Rm_{rms} < 1$ ), turbulent magnetic diffusivity grows rapidly with increasing velocity pulsations ( $\eta_t \sim \eta Rm_{rms}^2$ ). If the magnetic Reynolds number exceeds unity, the behavior of turbulent magnetic diffusivity becomes similar to the behavior of turbulent viscosity. The highest values of turbulent magnetic diffusivity are achieved at the end of braking, which corresponds to the transient stage of a strongly anisotropic turbulent flow in which the poloidal velocity oscillations prevail.

DOI: [10.1103/PhysRevE.85.016303](https://doi.org/10.1103/PhysRevE.85.016303)

PACS number(s): 47.35.Tv, 47.27.Jv, 47.27.tb

**I. INTRODUCTION**

The fully developed turbulent flow at very high Reynolds number (say,  $Re = VL/\nu \approx 10^6$  or more, where  $V$  is the typical large-scale velocity,  $L$  is a scale, and  $\nu$  is viscosity) cannot be obtained by direct numerical simulation of the Navier-Stokes equations. Therefore, different kinds of mean-field models are generally used to describe the behavior of large-scale fields. To overcome the closure problem, these models introduce effective (turbulent) transport coefficients, of which turbulent viscosity is the most well known [1,2].

For conducting fluids, the turbulent transport of magnetic fields is of primary interest. Small-scale turbulence may contribute to both the diffusion of magnetic fields and their generation [3,4]. The magnetic Reynolds number  $Rm = VL/\eta$  (where  $\eta$  is the magnetic diffusivity) characterizes the efficiency of hydrodynamic induction mechanism and is the parameter that defines the threshold of a hydromagnetic dynamo. The ratio of two Reynolds numbers gives the magnetic Prandtl number,  $Pm = Rm/Re = \nu/\eta$ , which, for liquid metals, is extremely small (of the order of  $10^{-5}$  and less). This means that the dynamo threshold (typically, of the order of a few tens) can be reached in fully turbulent flows only.

Over the past decade, substantial effort has been directed toward the study of the magnetohydrodynamic (MHD) dynamo in laboratory experiments (for a review, see Ref. [5]). The first-generation dynamo experiments were designed on the basis of strictly specified large-scale flows. In Ref. [6] the dynamo was generated by a cylindrical screw flow. The dynamo studied in Ref. [7], defined as a two-scale dynamo, was driven by a set of rigidly constrained helical jets inside

52 tubes. In this sense, these laboratory dynamos can be classified as quasilinear (despite that, the Reynolds numbers reached about  $10^7$ ) in which the role of turbulence was reduced to a strong enhancement of momentum diffusion and to a much weaker but notable enhancement of magnetic-field diffusion, which at constant magnetic permeability can be considered as an increase in the effective resistance of a liquid metal. The von Kármán sodium experiment in Ref. [8] was designed as a dynamo based on a mean flow generated by two counterrotating disks, but revealed a variety of dynamo regimes, in which the role of the turbulence is not yet completely understood [9]. However, the growth of resistivity can be crucial for any dynamo experiments because of the corresponding reduction in the magnetic Reynolds number.

Direct measurements of turbulent magnetic diffusion, as well as direct measurements of turbulent viscosity, are impeded in dynamo experiments by numerous side effects, which makes it difficult to isolate these effects. Therefore, in the study of MHD-transport coefficients, the subcritical flows of liquid metals are of main interest. Namely, we are interested in the turbulent flows characterized by the high Reynolds number and the moderate magnetic Reynolds numbers, i.e.,  $1 < Rm < Rm_*$ , where  $Rm_*$  denotes the dynamo threshold.

A method for designing high-Reynolds-number flows (although, nonstationary) in the limited mass of liquids has been proposed in Ref. [10], in which the flow was generated by the abrupt braking of a fast-rotating toroidal channel. Installation of diverters in the channel made it possible to create a toroidal screw flow of liquid metal that is potentially capable of generating a dynamo [11,12].

The spin-down flow of this type has been realized inside a toroidal channel made of textolite and filled with liquid gallium [13]. The large radius of the torus  $R = 0.0875$  m, the small radius of the torus  $r_0 = 0.0225$  m, and the net mass of liquid metal was 5.6 kg. The channel rotation rate  $\Omega$  reached

\*frick@icmm.ru

55 rps and yielded a Reynolds number of the order of  $10^6$ . The Reynolds number was based on the radius of the channel cross section and the initial toroidal speed. For gallium, the magnetic Prandtl number, defining the ratio of kinematic viscosity to magnetic diffusivity,  $Pm = \nu/\eta = 1.5 \times 10^{-6}$ . Therefore, the magnetic Reynolds number remained essentially less than unity. Even at such a relatively low magnetic Reynolds numbers the screw spin-down gallium flow allowed one to observe the  $\alpha$  effect produced by a joint action of the gradient of turbulent pulsations and large-scale vorticity [14]. The study of the dynamics of the *no-screw* spin-down flow of gallium in this torus has shown that the development of the flow in the channel is attended by a strong short-time burst of turbulent pulsations with a peak in the range 500–1000 Hz [15]. This burst of small-scale turbulence provides an opportunity to detect an approximately 1% increase in the effective resistivity of liquid metal [16].

The use of a similar experimental setup but with a titanium toroidal channel of larger size and filled with sodium made it possible to increase the magnetic Reynolds number by two orders of magnitude. It was found that at the maximal rotation rate  $\Omega = 45$  rps, corresponding to  $Rm \approx 30$ , in the case of the sodium spin-down flow the maximal deviation of magnetic diffusivity from its laminar value reaches about 50% [17].

In this paper we present an experimental study of velocity pulsations in the same *no-screw* spin-down flow of liquid sodium as described in Ref. [17]. We analyze the onset of the flow, the transient stage characterized by very sharp bursts of turbulent pulsations, and the decay of the turbulent flow. We estimate turbulent viscosity at all stages of flow evolution and compare the behavior of turbulent magnetic diffusivity and turbulent viscosity.

## II. EXPERIMENTAL SETUP

The setup is a construction mounted on a rigid frame used as a support for the rotating toroidal channel made of titanium alloy [17]. The torus radius  $R = 0.18$  m and the radius of the channel cross section  $r_0 = 0.08$  m. The channel is filled with sodium in vacuum and placed in an air thermostat. The channel temperature can be stabilized in the range 50–150 °C. A temperature sensor is mounted inside the channel and has good thermal contact with sodium in both the liquid and solid states.

The channel is fastened to the horizontal axis, which is also used for mounting a driving pulley, a system of sliding contacts, and a disk braking system. The rotation frequency of the channel is up to 50 rps and the flow in the channel is generated by abrupt braking. The braking time does not exceed 0.3 s. The flow velocity reaches a maximum after the channel stops and its toroidal component constitutes almost 70% of the linear velocity of the channel before braking. This means that the Reynolds number  $Re = Vr_0/\nu$  increases to  $Re \approx 3 \times 10^6$  at the most, which corresponds to the magnetic Reynolds number  $Rm \approx 30$ .

For velocity measurements, we use a two-axis local probe designed to ensure good dynamical resolution of toroidal and poloidal motion in liquid metals [15]. The probe schematic and its position in the channel are shown in Fig. 1. A small permanent magnet of size  $2 \times 2 \times 10$  mm<sup>3</sup> is used to

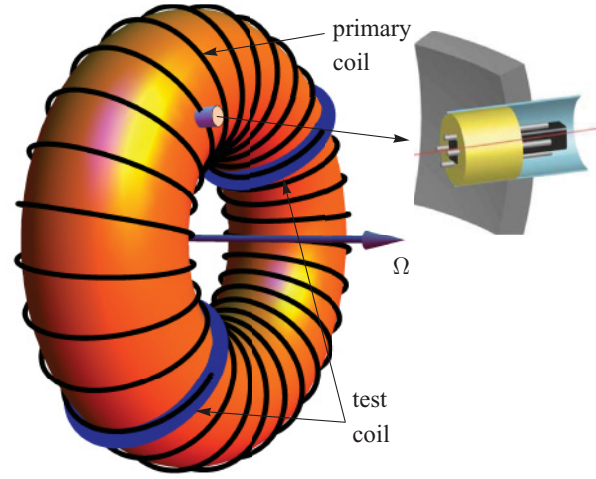


FIG. 1. (Color online) Torus channel with the coils wound around and the schematic of the potential probe. The permanent NdFeB magnet (size  $2 \times 2 \times 10$  mm<sup>3</sup>, in black) imposes a 2-kG magnetic field at the surface. Four electrodes are made of tinned copper wires (with a diameter of 0.8 mm) and allow a two-axis measurement of the velocity in the plane perpendicular to the magnet axis ( $v_x, v_y$ ).

locally apply a strong (2kG at the surface) magnetic field  $\mathbf{B} = B_0 \mathbf{e}_z$  and the nearby tinned copper electrodes of radius 0.8 mm are used to measure the induced electric potential difference related to the local velocity of the fluid by Ohm's law  $\mathbf{j} = \sigma(\mathbf{E} + \mathbf{v} \times \mathbf{B})$ . The potential difference between two electrodes yields the average velocity

$$\varphi_{x1} - \varphi_{x2} = \int v_y B_z dx. \quad (1)$$

Electric potential measurement can give an inaccurate determination of velocity for large  $Rm$ , caused by a drift of the probe magnetic field. Figure 2 shows the growth of the potential difference during the braking. At the beginning the fluid moves as a solid body and the relative velocity should be proportional to the decrease of rotation rate. The potential difference deviates from linear behavior for  $\Omega_s > 20$  rps (which corresponds to a velocity of about 23 m/s). However, such deviations can be caused also by the actual flow slowdown

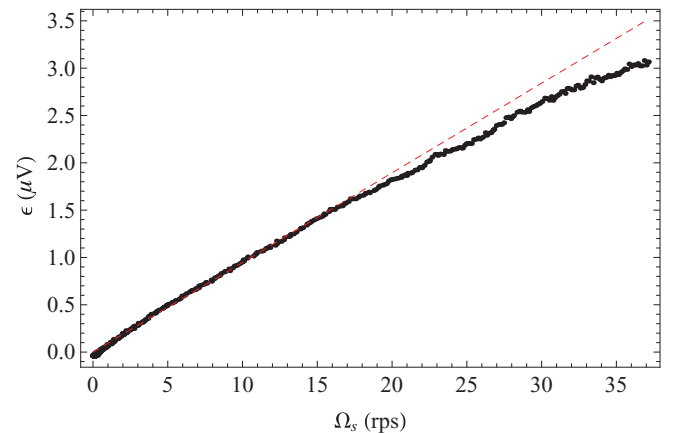


FIG. 2. (Color online) Potential difference vs assumed solid body rotation  $\Omega_s = \Omega_0 - \Omega(t)$  during braking. The dashed line shows a linear trend.

due to turbulence development. In any case, the inaccuracy is below 3% for velocities up to 20 m/s and does not exceed 15% for  $v = 45$  m/s.

Hence the spatial resolution of the measurement is provided by the electrode spacing and, consequently, the size of the magnet. The velocity is also averaged over the length of the electrode (as in conventional hot-wire anemometry). This is important because, even if the probe is mounted on the wall, the measurement is not performed within the boundary layer, whose thickness is less than  $10 \mu\text{m}$  compared to the top of the electrode immersed to a depth of approximately 1 mm in the fluid. The probe is mounted on the channel wall and sticks out inside the channel by 1.5 mm so that the measurements are done away from the boundary layers for any phase of the nonstationary flow evolution. Let us recall that in the case of a straight smooth pipe the averaged velocity reaches half of its value on the axis of the pipe at distance  $\approx 0.001r_0$  for  $\text{Re} \approx 10^6$  and at distance  $\approx 0.01r_0$  for  $\text{Re} \approx 10^5$  [1].

The primary (direct) output voltage is low, namely,  $106 \mu\text{V}/\text{m s}^{-1}$ . It is immediately fed into a differential amplifier AD8221 with a gain of 100, located inside the probe. The signal is then digitized using a 16-bit NI 9215 digitizer with a sampling frequency of 100 kHz. Based on the Taylor hypothesis (when applicable, i.e., if there is a mean flow), this probe can access large- and small-scale velocity fluctuations. Estimates in this flow (under traditional turbulence relationships) lead to Reynolds numbers of the order of  $\text{Re} \sim 10^6$ , with integral turbulent scale  $L \approx 0.1$  m and Kolmogorov's scale  $l_v \sim 10^{-5}$  m. At advection velocity  $U \sim 20$  m/s, this corresponds to the range of time frequencies  $200 < f < 10^6$  Hz. However, the smallest scale resolved by the probe is fixed by the electrode spacing corresponding to the upper frequency limit  $f_{\text{up}} \sim 40$  kHz.

The probe is mounted on the wall so that one of its axes is parallel to the local toroidal direction (along the channel) and the other axis is in the poloidal direction (Fig. 1). Thus we measure the local values of the toroidal  $v_{\text{tor}}$  and poloidal  $v_{\text{pol}}$  components of velocity.

The magnetic diffusivity of the metal inside the channel had been estimated by measuring the phase shift between the currents in two coils wound around the channel (see Fig. 1) [17]. A generator created in the toroidal coil a stabilized sinusoidal current with frequency  $30 < f < 1000$  Hz, which produced an alternating toroidal magnetic field inside the channel. Besides the toroidal coil, two diametrically located magnetic test coils were wound around the channel.

The change in the phase shift  $\theta$  between the magnetic flux through test coil and the alternating current in the toroidal coil is a value that can be treated as a measure of logarithmic changes of diffusivity of sodium [17],

$$\Delta\theta \simeq -C \frac{\Delta\sigma}{\sigma} = C \frac{\Delta\eta}{\eta}, \quad (2)$$

where  $C$  is a dimensional coefficient that depends on the geometry and resistivity of the channel wall and on the frequency of the applied magnetic field. The measured phase shift is determined by the variation of the conductivity of the metal and does not depend on large-scale distortions of the magnetic field by the flow because they do not change the total magnetic flux in the channel's cross section.

The measurement system has been tested and calibrated by measuring the temperature dependence of the sodium resistivity (see, for details, Ref. [17]). The channel filled with sodium was cooled down from  $105^\circ\text{C}$  to  $80^\circ\text{C}$ . This temperature range includes the sodium freezing point, which gives the best measure for calibration because the resistivity of sodium decreases at that point by 31%, while the temperature remains constant. This excludes the influence of resistivity variation of titanium, coils, etc. The theoretical phase shift in the skin layer of an infinite cylindrical solenoid [16], which includes a titanium cylinder tube with sodium, fits the experimental points well and allows us to define the factor of proportionality in Eq. (2) for each applied frequency. At  $f = 97$  Hz,  $C = 102 \pm 3$  mrad.

All dynamical experiments concerning the study of the turbulent flow of liquid sodium were performed at fixed temperature  $T = (102 \pm 1)^\circ\text{C}$ . The estimation of sodium heating caused by energy dissipation in the decaying turbulent flow at the highest rotational rate  $\Omega = 50$  rps, provided the entire kinetic energy is dissipated into heat, gives  $\Delta T \approx 0,8^\circ\text{C}$ , which corresponds to a variation in resistivity of less than 0.5%.

### III. FLOW EVOLUTION

We have performed more than 20 runs for each initial rotation rate of the torus ( $\Omega = 20, 30, 40,$  and  $50$  rps). The corresponding variations of the toroidal and poloidal velocities, averaged over 20 runs for each initial rotation rate, are shown in Fig. 3. It could be seen that at the first stage of braking the fluid toroidal velocity with respect to the halting vessel increases (as the probe is attached to the vessel, the measurement is performed in this initially moving frame of reference and the initial zero value of the fluid velocity corresponds to solid body rotation). The maximum of the toroidal fluid velocity is reached as the vessel stops and subsequent dynamics are measured in the frame at rest. In this process, a transverse (poloidal) velocity has been developed. The generation of poloidal velocity is provided by the curved channel and becomes more effective with increasing thickness of the torus  $r_0/R$ . In our case  $r_0/R = 0.44$  and for the maximal rotation rate  $\Omega = 50$  rps, at the end of braking the ratio of poloidal to toroidal mean velocities reaches  $U^{\text{pol}}/U^{\text{tor}} = 0.18$ . The maximal toroidal velocity  $U^{\text{tor}} = 0.69V_0 = 39$  m/s, where  $V_0$  is the velocity of the sodium on the channel axis before the brake. We can compare these results with the measurements made in the gallium flow [15]: The torus in the gallium experiment was thinner,  $r_0/R = 0.26$ , and the poloidal motion was weaker,  $(U^{\text{pol}}/U^{\text{tor}})_{\text{max}} = 0.08$ , while the toroidal motion remained stronger,  $U^{\text{tor}} = 0.80V_0$ .

Our main interest concerns the decaying stage of flow evolution. The decay starts at the end of braking and from here on we take the end of braking as a reference time point, i.e.,  $t = 0$  when the channel stops. Figure 4 shows the decay of the mean velocity on a log-log scale. The decay can be separated in two stages, transient and final. The final stage starts at  $t \approx 1.5\text{--}2$  s and displays a power-law decay for both velocity components  $U^{\text{tor}} \sim U^{\text{pol}} \sim t^{-1}$ . This law corresponds to a mean quadratic friction force  $dU/dt \sim -U^2$  and also satisfies

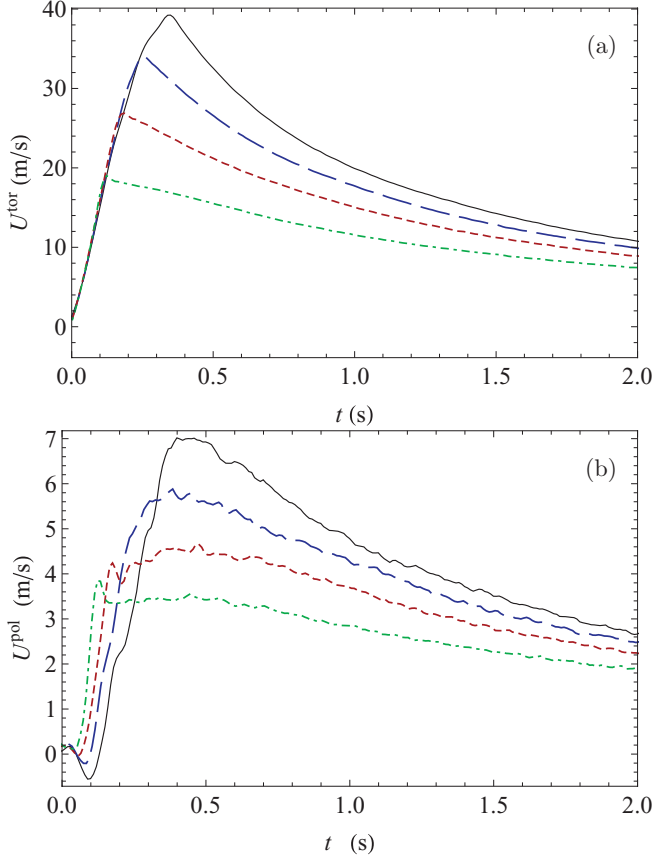


FIG. 3. (Color online) Evolution of the mean (a) toroidal and (b) poloidal velocities for  $\Omega = 20$  rps [dash-dotted (green) line], 30 rps [short-dashed (red) line], 40 rps [long-dashed (blue) line], and 50 rps [solid (black) line]. Each line is the result of averaging over 20 runs. Time  $t = 0$  corresponds to the beginning of braking.

the Kolmogorov picture of free decaying homogeneous turbulence with a fixed integral scale [ $d(U^2)/dt \approx -\varepsilon \approx -U^3 L$ , where  $\varepsilon$  is the energy dissipation rate].

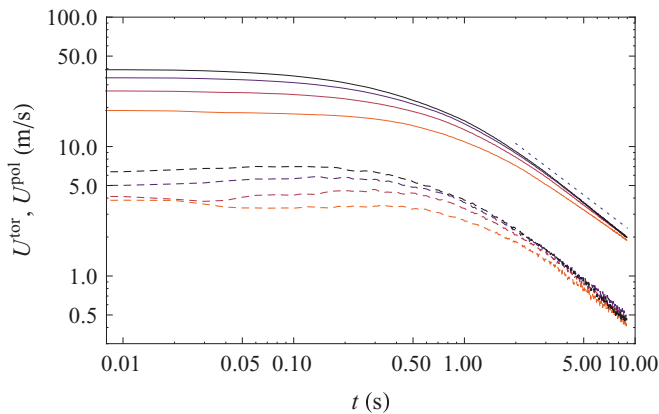


FIG. 4. (Color online) Decay of mean toroidal (solid lines) and poloidal (dashed lines) velocities in log-log coordinates. Here and in the following  $t = 0$  corresponds to the end of braking for  $\Omega = 20$ , 30, 40, and 50 rps (bottom-up, the lighter the color of the curve, the smaller the value of  $\Omega$ ). The dotted line corresponds to a power law  $t^{-1}$ .

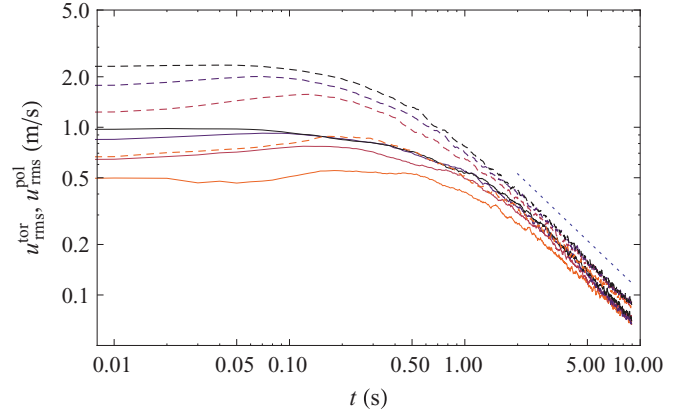


FIG. 5. (Color online) Temporal evolution of mean-root-square pulsations of the toroidal (solid lines) and poloidal (dashed lines) velocities for  $\Omega = 20$ , 30, 40, and 50 rps (bottom-up, the lighter the color of the curve, the smaller the value of  $\Omega$ ). The dotted line corresponds to a power law  $t^{-1}$ .

#### IV. SMALL-SCALE TURBULENCE DYNAMICS

In this section we discuss the characteristics of small-scale turbulence. Figure 5 illustrates the evolution of toroidal and poloidal pulsations, defined as the root-mean-square deviation from the corresponding mean velocity obtained by averaging over 20 individual runs. It could be seen that poloidal pulsations are stronger at the transient stage and both the poloidal and toroidal pulsations tend to the same power law of evolution as the mean flow, i.e.,  $u_{\text{rms}} \sim t^{-1}$ .

Figure 6 quantifies the tendency of the pulsation's evolution and shows the behavior of the turbulence level and the coefficient of anisotropy. The turbulence level is defined as  $u_{\text{rms}}^{\text{pol}}/U^{\text{tor}}$  and reaches its maximum near the end of the braking. During the transient stage, the turbulence level goes down and remains stable at the final stage of evolution, which means that in the decay the rms pulsations are proportional to the mean toroidal velocity. This is consistent with the analogous decay law for the mean velocity and pulsations. The maximum of the turbulence level coincides in time with the maximum of anisotropy [see Fig. 6(b)]. At this moment the poloidal pulsations exceed the toroidal pulsations by a factor of 2.4. At the late stage of evolution, the small constant anisotropy still remains valid ( $u_{\text{rms}}^{\text{pol}}/u_{\text{rms}}^{\text{tor}} \approx 1.2$ ), showing a weak dominance of poloidal pulsations in the domain of velocity measurements.

The wavelet transform of the time evolution of toroidal and poloidal components for  $\Omega = 50$  rps averaged over 20 realizations is shown in Fig. 7. As could be seen in the figure, the fluctuations at all scales increase rapidly as the channel is halted. The end of braking ( $t = 0$  in the figure) also corresponds to the widest spectral content with a maximum at about 2.5 kHz, followed by a long decay. Using these wavelet transforms, we have calculated the power spectral density of velocity fluctuations by summarizing the energy of the poloidal and toroidal velocities for a given frequency within a fixed interval of time. Figure 8(a) presents the power spectra for the sequence of time intervals  $0 < t < 0.5$ ,  $0.5 < t < 1.5$ ,  $1.5 < t < 3.5$ , and  $3.5 < t < 7.5$ . The time evolution of the

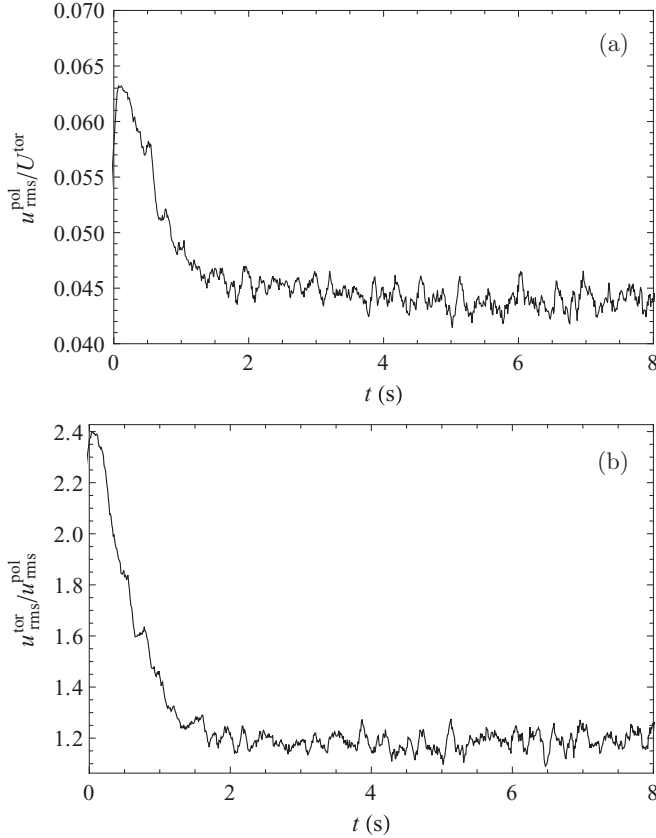


FIG. 6. Temporal evolution of (a) turbulence level defined as  $u_{\text{rms}}^{\text{pol}}/U^{\text{tor}}$  and (b) anisotropy of velocity fluctuations defined as  $u_{\text{rms}}^{\text{tor}}/u_{\text{rms}}^{\text{pol}}$  for  $\Omega = 50$  rps.

spectra indicates that the energy content is broadest at the time when the channel has stopped and the motions slow down with the development of a scaling region at later times. The dotted lines correspond to a Kolmogorov slope of  $-5/3$  within the high-frequency spectral range and to a slope of 1 in the low-frequency part. The picture is clearer in the spatial spectral space, constructed using the Taylor hypothesis at the local toroidal velocity [Fig. 8(b)]. In  $k$  space, the maximum of the spectral power is fixed at the scale corresponding to the length scale of  $2r_0$  equal to the channel diameter. At time exceeding 1.5 s, the spatial spectra show the range of scales consistent with a  $-5/3$  scaling characteristic of the decay of three-dimensional turbulence.

Finally, we calculate the cross correlation of pulsations of two measured velocity components  $\langle u^{\text{pol}}u^{\text{tor}} \rangle$ . Measurements for different directions of channel rotation show that the time evolution of the cross correlation strongly differs for clockwise and counterclockwise channel rotations. Figure 9(a) illustrates the evolution of the normalized cross correlation  $c^{\pm} = \langle u^{\text{pol}}u^{\text{tor}} \rangle / u_{\text{rms}}^{\text{pol}}u_{\text{rms}}^{\text{tor}}$ , where the plus sign index denotes the clockwise rotation and the minus sign index the counterclockwise rotation. These two curves are neither symmetric nor asymmetric. Note that the mean toroidal velocity  $U^{\text{tor}}$  changes the sign together with the direction of rotation, while the poloidal  $U^{\text{pol}}$  does not. To separate the input of two flow modes into the cross correlations, we plot the even and odd contributions, defined as  $c^{\text{even}} = (c^{+} + c^{-})/2$  and

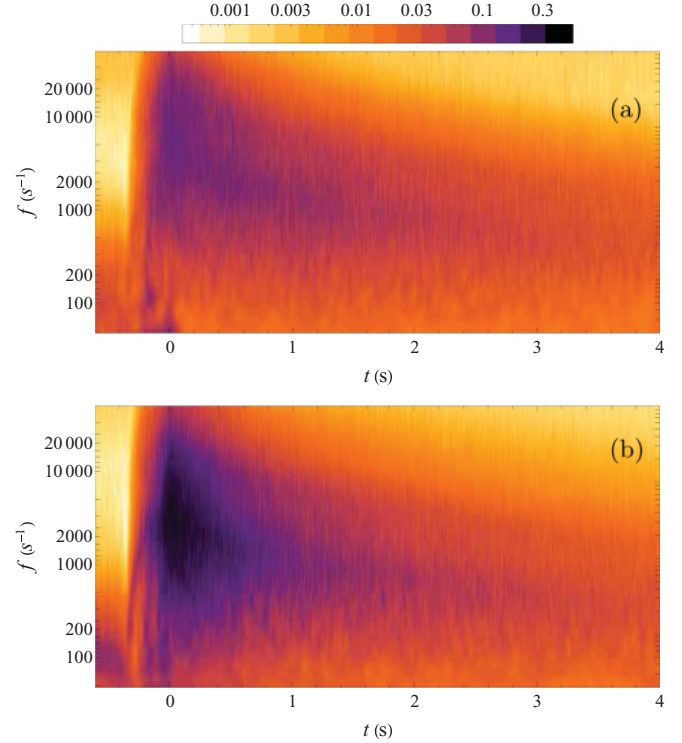


FIG. 7. (Color online) Wavelet spectrogram of velocity pulsations: (a) toroidal velocity and (b) poloidal velocity for  $\Omega = 50$  rps.

$c^{\text{odd}} = (c^{+} - c^{-})/2$  in Fig. 9(b). The even part, provided by the poloidal velocity field, is maximal during the braking and slowly decreases up to  $t \approx 1$  s. The odd part that can be attributed to the toroidal velocity field starts to increase after braking and reaches the value  $c^{-} \approx -0.35$ , which remains stable in the decay.

## V. TURBULENT TRANSPORT COEFFICIENTS

The turbulent viscosity  $\nu_t$  appears if the Reynolds stress tensor is written in a form similar to the form of the viscous stress tensor

$$\langle u_i u_j \rangle = \frac{\langle u_k^2 \rangle}{3} \delta_{ij} - \nu_t (\partial_j U_i + \partial_i U_j). \quad (3)$$

A crude estimate of the turbulent viscosity in a given flow can be obtained by assuming that  $\nu_t$  is constant throughout the flow. Then the Reynolds equation takes the form of the Navier-Stokes equation with some additional viscosity,

$$\partial_t \mathbf{U} + (\mathbf{U} \cdot \nabla) \mathbf{U} = -\rho^{-1} \nabla P + (\nu + \nu_t) \nabla^2 \mathbf{U}. \quad (4)$$

This hypothesis implies that the turbulent flow exactly reproduces the laminar solution with an amplified value of viscosity. For a straight pipe, it corresponds to the Poiseuille profile for the averaged velocity  $U(r) = 2V(1 - r^2/r_0^2)$  (where  $V$  is the mean velocity obtained from the flow rate  $Q = \pi r_0^2 V$ ). In this case,  $\tau = 4\rho\nu_t V/r_0$  is the stress on the wall. Considering the nonstationary flow in the channel as an inertial decelerating

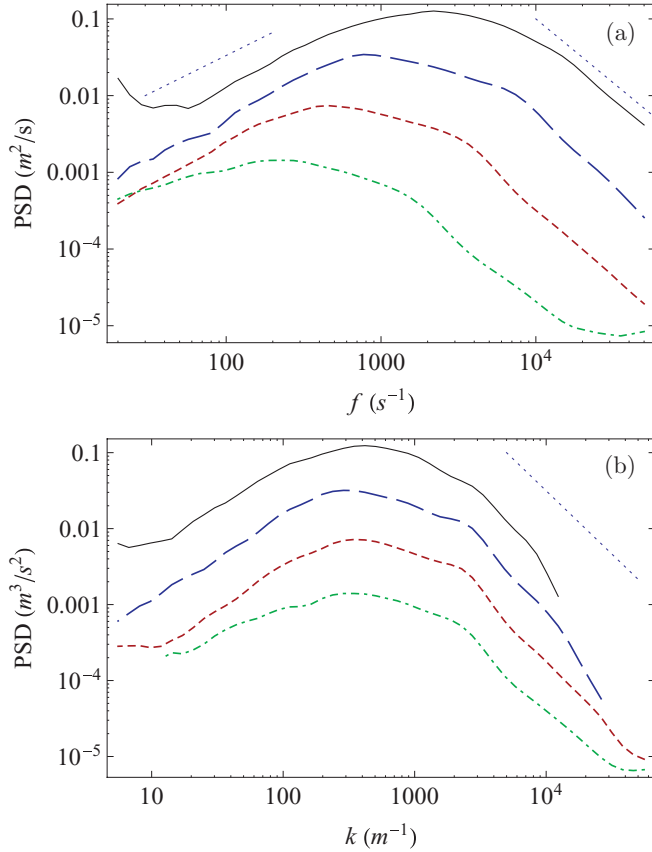


FIG. 8. (Color online) Power spectral density (PSD) of velocity fluctuations. (a) Time spectra obtained as the vertical cross section of the wavelet transforms shown in Fig. 7 averaged over time in the four intervals between  $t = 0, 0.5, 1.5, 3.5,$  and  $7.5$  s (from top to bottom). (b) Corresponding spectra of the spatial energy distribution. The dotted line corresponds to the Kolmogorov  $-5/3$  law for the inertial range and to  $E(\omega) \sim \omega$  for the low-frequency part of the spectrum.

motion of the fluid cylinder under the action of the wall friction ( $\pi r_0^2 \rho dV/dt = 2\pi r_0 \tau$ ), we get

$$v_t = \frac{r_0^2}{8V} \frac{dV}{dt}. \quad (5)$$

Under these assumptions, the time variation of the mean velocity  $U(r, t)$  in each point follows the variations of  $V(t)$  and thus Eq. (5) can be used to evaluate the turbulent viscosity from the measured toroidal velocity  $U^{\text{tor}}(t)$ .

To gain more sophisticated estimates of turbulent viscosity, we use the Kolmogorov-Prandtl expression [18]

$$v_t = C \frac{E_t^2}{\epsilon}, \quad (6)$$

where  $C$  is a dimensionless prefactor of the order of unity,  $E_t = (u_{\text{rms}}^{\text{pol}})^2$  is an estimation of the energy of turbulent pulsations, and  $\epsilon = \partial(U^{\text{tor}})^2/\partial t$  is an estimation of the kinetic energy dissipation rate.

Figure 10 shows the evolution of turbulent viscosity for different rotation rates. We present the results obtained from Eqs. (5) and (6). Equation (5) yields a strong overestimation of the effective (turbulent) viscosity because it implies a parabolic

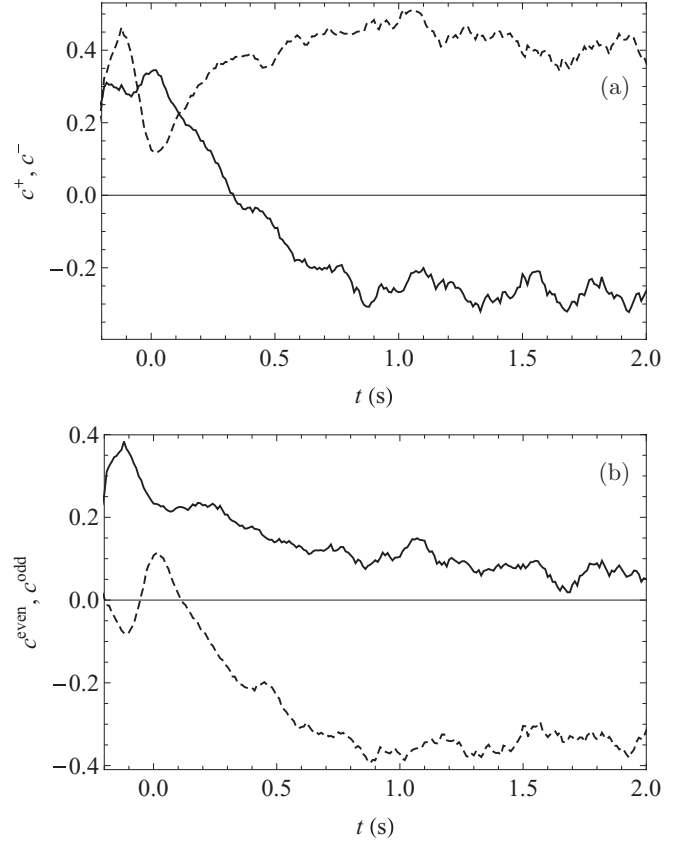


FIG. 9. (a) Normalized cross correlation  $\langle u^{\text{pol}} u^{\text{tor}} \rangle$  for clockwise  $c^+$  (solid line) and counterclockwise  $c^-$  (dashed line) channel rotation. (b) Symmetric  $c^{\text{even}}$  (solid line) and asymmetric  $c^{\text{odd}}$  (dashed line) parts of cross correlations for  $\Omega = 50$  rps.

velocity profile, which is obviously wrong for the Reynolds numbers under consideration. Nevertheless, both definitions provide similar behavior for the turbulent velocity, displaying a power-law decay at the late stage of evolution. For  $t > 1$  s, we get  $v_t \sim t^{-1.3}$  (the corresponding slope is shown in the figure by a dashed line).

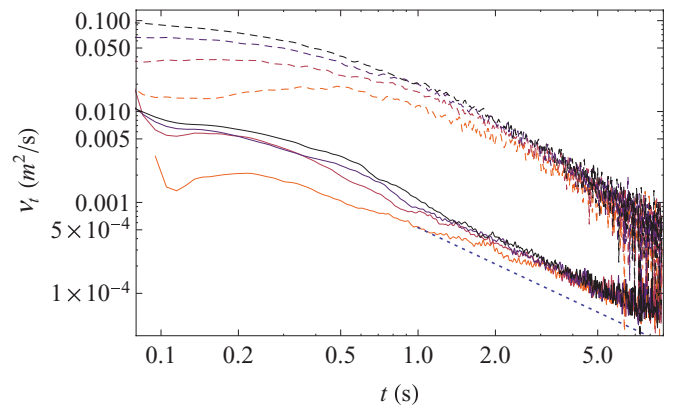


FIG. 10. (Color online) Evolution of turbulent viscosity, defined by Eq. (5) (top group of lines) and (6) (bottom group of lines) for different rotation rates:  $\Omega = 20, 30, 40,$  and  $50$  rps (bottom-up, the lighter the color of the curve, the smaller the value of  $\Omega$ ). The dashed line corresponds to a power law  $t^{-1.3}$ .

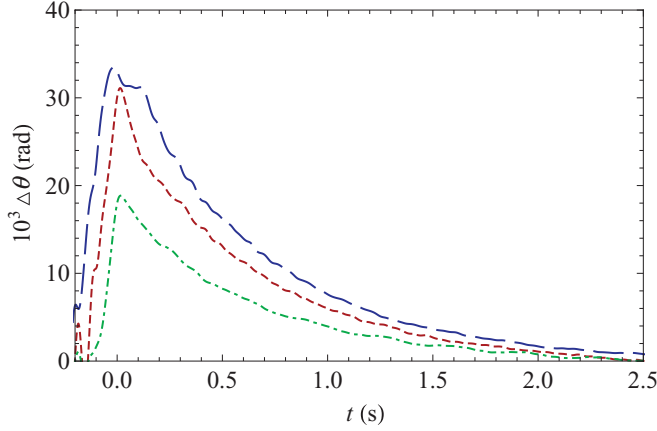


FIG. 11. (Color online) Variation of the phase shift between the applied and induced currents with flow evolution for a channel rotation rate  $\Omega = 20$  rps [dash-dotted (green) line], 30 rps [short-dashed (red) line], and 40 rps [long-dashed (blue) line]. The frequency of the applied alternating field  $f = 97$  Hz.

The evolution of the large-scale magnetic field in the turbulent flow of electrically conducting media can be described by the mean-field induction equations (see, e.g., Refs. [3,4]), which are derived by applying the Reynolds approach to the induction equation. In the simplest case of homogeneous and isotropic (but mirror asymmetric) turbulence, these equations can be reduced to

$$\partial_t \mathbf{B} = \nabla \times (\mathbf{U} \times \mathbf{B}) + \alpha \nabla \times \mathbf{B} + (\eta + \eta_t) \nabla^2 \mathbf{B}, \quad (7)$$

where  $\mathbf{B}$  corresponds to the mean (large-scale) magnetic fields and  $\alpha$  and  $\eta_t$  are the turbulent transport coefficients responsible for the action of small-scale turbulent pulsations on the mean-field dynamics. The coefficient  $\alpha$  describes the generation effects and  $\eta_t$  describes the contribution of turbulence to the diffusion of the large-scale magnetic field and a close analog of the turbulent viscosity  $\nu_t$ .

In our experiments, the indicator of an increase in magnetic diffusivity is the phase shift between the induced and applied alternating magnetic fields. Figure 11 illustrates the evolution of the phase shift measured as described above. The general shapes of the curves are similar to the curves characterizing the evolution of the turbulent spin-down flow, which supports the conclusion that the effect is produced by the action of the turbulent flow.

Let us now construct the plot of the phase shift versus rms velocity pulsation for different rotation rates (lower curves, shown by thick lines in Fig. 12). Note again that the measured phase shift corresponds to the averaged magnetic diffusivity in the whole mass of liquid sodium, while the velocity measurements are done at one fixed point of the flow. However, apart from the transient stage of evolution that corresponds to the hook in the upper part of each curve, the data obtained from different runs lie on the same line, showing that the phase shift is defined by the intensity of turbulent pulsations. The turbulent viscosity evaluated by Eq. (6) is shown by the thin (upper) lines in Fig. 12. For the decaying stage of evolution, the results obtained at different initial rotation rates of the channel are very close and display a pronounced power-law

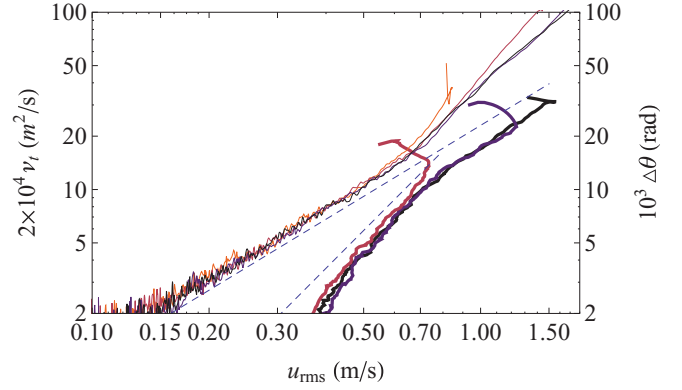


FIG. 12. (Color online) Turbulent viscosity (thin upper lines) and turbulent magnetic diffusivity (thick lower lines) versus root-mean-square velocity fluctuations for  $\Omega = 20, 30, 40$ , and 50 rps (bottom-up, the lighter the color of the curve, the smaller the value of  $\Omega$ ). Two dashed lines correspond to power laws  $u_{\text{rms}}^{1.3}$  (top) and  $u_{\text{rms}}^2$  (bottom).

dependence on the intensity of turbulent pulsations, namely,  $\nu_t \sim u_{\text{rms}}^{1.3}$ . This slope is shown in Fig. 12 by the top dashed line. The slope increases only at the highest values of  $u$ , which corresponds to the strongly nonstationary and anisotropic stage of evolution.

The effective magnetic diffusivity shows different behavior at low and high levels of turbulent pulsations. At low  $u_{\text{rms}}$ , diffusivity increases much faster than viscosity and at high  $u_{\text{rms}}$ , the slope for diffusivity tends to the slope for viscosity, i.e.,  $\eta_t \sim u_{\text{rms}}^{1.3}$ . To explain this transition from one power law to another, we introduce the magnetic Reynolds number, defined via the rms velocity pulsations,

$$\text{Rm}_{\text{rms}} = \frac{u_{\text{rms}} r_0}{\eta}.$$

Such a definition of the magnetic Reynolds number is more suitable for the analysis of the behavior of turbulent magnetic diffusivity because the increase in effective diffusivity can be attributed to small-scale turbulent pulsations. In our case,  $r_0 = 0.08$  m and  $\eta = 0.078$  m<sup>2</sup> s<sup>-1</sup>, thus  $\text{Rm}_{\text{rms}}$  is approximately equal to the rms velocity pulsations given in m/s; Fig. 12 shows that the behavior of turbulent magnetic diffusivity changes near the point  $\text{Rm}_{\text{rms}} \approx 0.8$ .

The magnetic energy dissipation rate  $\epsilon_B$  provided by the turbulence is directly related to the power spectral density of magnetic-field fluctuations  $E_B(k)$  [19],

$$\epsilon_B = \eta \int_0^\infty k^2 E_B(k) dk. \quad (8)$$

The direct measurement of local magnetic-field fluctuations was unfortunately beyond the facilities of the experiment. However, the magnetic dissipation scale  $k_\eta \approx (\epsilon/\eta^3)^{1/4} \approx 10$ ; this means that the whole range covered by the spectrum of kinetic energy ( $k_L < k < k_v$ ) includes only  $k > k_\eta$  ( $l_\eta = 2\pi/k_\eta > 2R$ ). This allows us to relate the magnetic power spectral density to kinetic power spectral density

$$E_B(k) \sim \frac{B_0^2}{\eta^2} \frac{E_V(k)}{k^2}. \quad (9)$$

Here  $B_0$  is the applied magnetic field. Equation (9) implies that the spectrum of magnetic pulsations is governed by the balance of induction provided by velocity fluctuations and the Ohmic dissipation and is valid for a weak induced magnetic field (small  $Rm$ ). Supposing the Kolmogorov  $-5/3$  power law for the kinetic-energy spectrum, one gets from Eq. (9) the well-known  $-11/3$  spectrum for the magnetic energy, predicted by Golitsyn [20] and Moffat [19] and observed in various turbulent MHD flows under low  $Rm$  (see, e.g., Ref. [21]). Combining Eqs. (8) and (9) we get

$$\epsilon_B \approx \frac{B_0^2}{\eta} \int_{k_L}^{\infty} E_V(k) dk \approx \frac{B_0^2}{\eta} u_{\text{rms}}^2 = \frac{\eta B_0^2}{r_0^2} Rm_{\text{rms}}^2. \quad (10)$$

The dependence  $\epsilon_B \propto Rm^2$  for the turbulent magnetic diffusivity (the beta effect) in the limit of small  $Rm$  is known from the mean-field approximation [3,4]. In Fig. 12 this power law is shown by the bottom dashed line. We see that for  $Rm_{\text{rms}} < 1$  the turbulent magnetic diffusivity really follows the law

$$\eta_t \sim \eta Rm_{\text{rms}}^2,$$

excluding the lowest measured values (at  $Rm_{\text{rms}} < 0.4$  the curves are steeper).

## VI. CONCLUSION

The spin-down flow in the abruptly halted torus is nonstationary and its evolution includes three stages. At the initial stage of flow formation, the inertial force generates the basic toroidal flow, whose instability gives rise to the poloidal mode. This stage is followed by the transient regime, characterized by strong anisotropy, i.e., the dominance of poloidal velocity pulsations. The last stage is the free self-similar decay of turbulence, which is characterized by Kolmogorov's inertial range and a power-law decay of kinetic energy. A weak anisotropy of pulsations still remains valid at this stage.

It is obvious that the three-dimensional flow pattern is fairly complicated and changes during the evolution of the flow, which implies a complex spatial distribution of the effective transport coefficients for the momentum (turbulent viscosity) and for the magnetic field (turbulent magnetic diffusivity). Let us emphasize that the turbulent transport coefficients are evaluated using two different kinds of measurements: the measurement of the velocity at one fixed point in the

vicinity of the wall and the measurement of the inductance of the coil wound around the channel. This allowed us to determine the mean effective magnetic diffusivity of sodium inside the channel. Thus the velocity measurements are *local* and the magnetic-field measurements are *global*, which requires caution with the comparison of the results of corresponding estimations.

It should be noted that the previous measurements of effective magnetic diffusivity in spin-down flows have not been supported by velocity pulsation measurements [16,17]. The increase in magnetic diffusivity has been analyzed as a function of the rotation rate of the channel. It has been found that the maximal deviation of magnetic diffusivity in the nonstationary flow increases with increasing channel rotation rate  $\Omega$ . In the gallium experiment ( $Rm \ll 1$ ), the increase in magnetic diffusivity fits a parabola ( $\max\{\eta_t\} \sim \Omega^2$ ) [16]. In the sodium experiment, at low  $\Omega$ , the increase looks linear,  $\max\{\eta_t\} \sim \Omega$ , and tends to the root-square dependence at the highest rotation rates ( $\max\{\eta_t\} \sim \sqrt{\Omega}$ ) [17].

The two-component velocity probe, installed on the channel wall, allowed us to relate the evolution of the effective magnetic diffusivity to the evolution of the turbulent flow. It is shown that, in the late (self-similar) decay of the turbulent flow, the turbulent viscosity depends on the rms velocity pulsations as  $\nu_t \sim \nu Re_{\text{rms}}^{1.3}$ . The behavior of turbulent magnetic diffusivity depends then on the magnetic Reynolds numbers, defined via the rms velocity pulsations. At small magnetic Reynolds number ( $Rm_{\text{rms}} < 1$ ), the turbulent magnetic diffusivity grows rapidly with increasing velocity pulsations ( $\eta_t \sim \eta Rm_{\text{rms}}^2$ ). If the magnetic Reynolds number exceeds unity, the behavior of the turbulent magnetic diffusivity becomes similar to the behavior of turbulent viscosity. The highest values of turbulent magnetic diffusivity are achieved at the end of braking and the time interval (about 1 s after braking), analyzed in Ref. [17], corresponds to the transient stage with a strongly anisotropic turbulent flow with dominating poloidal velocity oscillations.

## ACKNOWLEDGMENTS

This work was supported by the International Scientific Technological Center (Project No. 3726) and the Russian Foundation for Basic Research (Project No. 11-01-00423a).

- 
- [1] H. Schlichting, *Grenzschicht-Theories* (Braun, Karlsruhe, 1964).
  - [2] P. A. Davidson, *Turbulence: An Introduction for Scientists and Engineers* (Oxford University Press, Oxford, UK, 2004).
  - [3] H. K. Moffatt, *Magnetic Field Generation in Electrically Conducting Fluids* (Cambridge University Press, Cambridge, 1978).
  - [4] F. Krause and K.-H. Rädler, *Mean-Field Magnetohydrodynamics and Dynamo Theory* (Pergamon, New York, 1980).
  - [5] F. Stefani, A. Gailitis, and G. Gerbeth, *Z. Angew. Math. Mech.* **88**, 930 (2008).
  - [6] A. Gailitis *et al.*, *Phys. Rev. Lett.* **84**, 4365 (2000).
  - [7] R. Stieglitz and U. Müller, *Phys. Fluids* **13**, 561 (2001).
  - [8] R. Monchaux *et al.*, *Phys. Rev. Lett.* **98**, 044502 (2007).
  - [9] F. Pétrélis, N. Mordant, and S. Fauve, *Geophys. Astrophys. Fluid Dyn.* **101**, 289 (2007).
  - [10] P. Frick, V. Noskov, S. Denisov, S. Khripchenko, D. Sokoloff, R. Stepanov, and A. Sukhanovsky, *Magnetohydrodynamics* **38**, 143 (2002).
  - [11] W. Dobler, P. Frick, and R. Stepanov, *Phys. Rev. E* **67**, 056309 (2003).
  - [12] A. Chupin, P. Frick, and R. Stepanov, *Astron. Nachr.* **332**, 11 (2011).
  - [13] V. Noskov, S. Denisov, P. Frick, S. Khripchenko, D. Sokoloff, and R. Stepanov, *Eur. Phys. J. B* **41**, 561 (2004).

- [14] R. Stepanov, R. Volk, S. Denisov, P. Frick, V. Noskov, and J. F. Pinton, *Phys. Rev. E* **73**, 046310 (2006).
- [15] V. Noskov, R. Stepanov, S. Denisov, P. Frick, G. Verhille, N. Plihon, and J. Pinton, *Phys. Fluids* **21**, 045108 (2009).
- [16] S. A. Denisov, V. I. Noskov, R. A. Stepanov, and P. G. Frick, *JETP Lett.* **88**, 167 (2008).
- [17] P. Frick, V. Noskov, S. Denisov, and R. Stepanov, *Phys. Rev. Lett.* **105**, 184502 (2010).
- [18] S. B. Pope, *Turbulent Flows* (Cambridge University Press, Cambridge, 2000).
- [19] H. K. Moffatt, *J. Fluid Mech.* **11**, 625 (1961).
- [20] G. S. Golitsyn, *Sov. Phys. Dokl.* **5**, 536 (1960).
- [21] P. Odier, J.-F. Pinton, and S. Fauve, *Phys. Rev. E* **58**, 7397 (1998).